Resolution and contrast enhancement in laser scanning microscopy using dark beam imaging

Harold Dehez,[1,2] Michel Piché,[2] and Yves De Koninck[1,*]

[1]*Institut universitaire en santé mentale de Québec, 2601 chemin de la Canardière, Québec, QC, G1J2G3, Canada*
[2]*Centre d'optique, photonique et laser, Université Laval, 2375 rue de la Terrasse Québec, QC, G1V0A6, Canada*
[*]*yves.dekoninck@crulrg.ulaval.ca*

Abstract: Laser scanning microscopy allows for three-dimensional imaging of cells with molecular specific labeling. However the spatial resolution of optical microscopy is fundamentally limited by the diffraction of light. In the last two decades many techniques have been introduced to enhance the resolution of laser scanning microscopes. However most of these techniques impose strong constraints on the specimen or rely on complex optical systems. These constraints limit the applicability of resolution improvement to various imaging modalities and sample types. To overcome these limitations, we introduce here a novel approach, which we called Switching LAser Mode (SLAM) microscopy, to enhance resolution and contrast in laser scanning microscopy. SLAM microscopy relies on subtracting images obtained with dark and bright modes, and exploits the smaller dimensions of the dark spot of the azimuthally polarized TE_{01} mode. With this approach, resolution is improved by a factor of two in confocal microscopy. The technique is not based on complex nonlinear processes and thus requires laser power similar to that used in conventional imaging, minimizing photo-damage. The flexibility of the approach enables retrofitting in commercial confocal and two-photon microscopes and opens avenues for resolution enhancement in fluorescence-independent microscopy.

OCIS codes: (140.3300) Laser beam shaping; (180.5810) Scanning microscopy; (180.1790) Confocal microscopy; (180.4315) Nonlinear microscopy; (350.5730) Resolution.

References and links

1. A. Yildiz, J. N. Forkey, S. A. McKinney, T. Ha, Y. E. Goldman, and P. R. Selvin, "Myosin V walks hand-over-hand: single fluorophore imaging with 1.5-nm localization," Science **300**(5628), 2061–2065 (2003).
2. E. Betzig, G. H. Patterson, R. Sougrat, O. W. Lindwasser, S. Olenych, J. S. Bonifacino, M. W. Davidson, J. Lippincott-Schwartz, and H. F. Hess, "Imaging intracellular fluorescent proteins at nanometer resolution," Science **313**(5793), 1642–1645 (2006).
3. M. J. Rust, M. Bates, and X. Zhuang, "Sub-diffraction-limit imaging by stochastic optical reconstruction microscopy (STORM)," Nat. Methods **3**(10), 793–796 (2006).
4. S. T. Hess, T. P. Girirajan, and M. D. Mason, "Ultra-high resolution imaging by fluorescence photoactivation localization microscopy," Biophys. J. **91**(11), 4258–4272 (2006).
5. H. Balci, T. Ha, H. L. Sweeney, and P. R. Selvin, "Interhead distance measurements in myosin VI via SHRImP support a simplified hand-over-hand model," Biophys. J. **89**(1), 413–417 (2005).
6. H. Shroff, C. G. Galbraith, J. A. Galbraith, and E. Betzig, "Live-cell photoactivated localization microscopy of nanoscale adhesion dynamics," Nat. Methods **5**(5), 417–423 (2008).
7. S. A. Jones, S. H. Shim, J. He, and X. Zhuang, "Fast, three-dimensional super-resolution imaging of live cells," Nat. Methods **8**(6), 499–505 (2011).
8. L. Shao, P. Kner, E. H. Rego, and M. G. Gustafsson, "Super-resolution 3D microscopy of live whole cells using structured illumination," Nat. Methods **8**(12), 1044–1046 (2011).
9. R. Fiolka, L. Shao, E. H. Rego, M. W. Davidson, and M. G. Gustafsson, "Time-lapse two-color 3D imaging of live cells with doubled resolution using structured illumination," Proc. Natl. Acad. Sci. U.S.A. **109**(14), 5311–5315 (2012).
10. G. Donnert, J. Keller, R. Medda, M. A. Andrei, S. O. Rizzoli, R. Lührmann, R. Jahn, C. Eggeling, and S. W. Hell, "Macromolecular-scale resolution in biological fluorescence microscopy," Proc. Natl. Acad. Sci. U.S.A. **103**(31), 11440–11445 (2006).

#188025 - $15.00 USD Received 1 Apr 2013; revised 31 May 2013; accepted 31 May 2013; published 25 Jun 2013

11. R. Kasper, B. Harke, C. Forthmann, P. Tinnefeld, S. W. Hell, and M. Sauer, "Single-molecule STED microscopy with photostable organic fluorophores," Small **6**(13), 1379–1384 (2010).
12. G. Vicidomini, G. Moneron, K. Y. Han, V. Westphal, H. Ta, M. Reuss, J. Engelhardt, C. Eggeling, and S. W. Hell, "Sharper low-power STED nanoscopy by time gating," Nat. Methods **8**(7), 571–573 (2011).
13. R. Dorn, S. Quabis, and G. Leuchs, "Sharper focus for a radially polarized light beam," Phys. Rev. Lett. **91**(23), 233901 (2003).
14. J. Kim, D. C. Kim, and S. H. Back, "Demonstration of high lateral resolution in laser confocal microscopy using annular and radially polarized light," Microsc. Res. Tech. **72**(6), 441–446 (2009).
15. Y. Kozawa, T. Hibi, A. Sato, H. Horanai, M. Kurihara, N. Hashimoto, H. Yokoyama, T. Nemoto, and S. Sato, "Lateral resolution enhancement of laser scanning microscopy by a higher-order radially polarized mode beam," Opt. Express **19**(17), 15947–15954 (2011).
16. J. Stadler, C. Stanciu, C. Stupperich, and A. J. Meixner, "Tighter focusing with a parabolic mirror," Opt. Lett. **33**(7), 681–683 (2008).
17. O. Haeberlé and B. Simon, "Saturated structured confocal microscopy with theoretically unlimited resolution," Opt. Commun. **282**(18), 3657–3664 (2009).
18. B. R. Boruah, "Lateral resolution enhancement in confocal microscopy by vectorial aperture engineering," Appl. Opt. **49**(4), 701–707 (2010).
19. S. N. Khonina and I. Golub, "How low can STED go? Comparison of different write-erase beam combinations for stimulated emission depletion microscopy," J. Opt. Soc. Am. A **29**(10), 2242–2246 (2012).
20. B. Richards and E. Wolf, "Electromagnetic diffraction in optical systems. 2. Structure of the image field in an aplanatic system," Proc. R. Soc. A **253**, 358–379 (1959).
21. L. Novotny and B. Hecht, *Principles of Nano-Optics*, (Cambridge University, 2007).
22. H. Dehez, M. Piché, and Y. De Koninck, "Enhanced resolution in two-photon imaging using a TM_{01} laser beam at a dielectric interface," Opt. Lett. **34**(23), 3601–3603 (2009).
23. T. A. Pologruto, B. L. Sabatini, and K. Svoboda, "ScanImage: flexible software for operating laser scanning microscopes," Biomed. Eng. Online **2**(1), 13 (2003).
24. D. Débarre, W. Supatto, A. M. Pena, A. Fabre, T. Tordjmann, L. Combettes, M. C. Schanne-Klein, and E. Beaurepaire, "Imaging lipid bodies in cells and tissues using third-harmonic generation microscopy," Nat. Methods **3**(1), 47–53 (2006).
25. E. Bélanger, S. Bégin, S. Laffray, Y. De Koninck, R. Vallée, and D. Côté, "Quantitative myelin imaging with coherent anti-Stokes Raman scattering microscopy: alleviating the excitation polarization dependence with circularly polarized laser beams," Opt. Express **17**(21), 18419–18432 (2009).
26. A. Hudmon, E. Lebel, H. Roy, A. Sik, H. Schulman, M. N. Waxham, and P. De Koninck, "A mechanism for Ca^{2+}/calmodulin-dependent protein kinase II clustering at synaptic and nonsynaptic sites based on self-association," J. Neurosci. **25**(30), 6971–6983 (2005).
27. S. Kredel, F. Oswald, K. Nienhaus, K. Deuschle, C. Röcker, M. Wolff, R. Heilker, G. U. Nienhaus, and J. Wiedenmann, "mRuby, a bright monomeric red fluorescent protein for labeling of subcellular structures," PLoS ONE **4**(2), e4391 (2009).
28. A. Diaspro, *Confocal and Two-Photon Microscopy: Foundations, Applications, and Advances*, (Wiley-Liss, 2002).
29. C. Labrakakis, L. E. Lorenzo, C. Bories, A. Ribeiro-da-Silva, and Y. De Koninck, "Inhibitory coupling between inhibitory interneurons in the spinal cord dorsal horn," Mol. Pain **5**(1), 24 (2009).

1. Introduction

In the last twenty years, several approaches have been proposed to enhance the resolution of optical microscopes. These techniques can be classified into two categories. The first category relies on single molecule imaging [1] using stochastic photoswitching or bleaching [2–5]. Such techniques are simple to implement in a widefield microscope, yielding an impressive resolution of ~20 nm. However, these approaches rely on specific properties of fluorescent probes (photo-switchable, high emission of photons before the dark state, low dark state emission). They also yield limited temporal resolution because sufficient statistics need to be acquired [6,7].

The second category relies on optical shaping of the excitation; it includes structured illumination microscopy and stimulated emission depletion (STED) microscopy. Structured illumination relies on multiple acquisitions to extract information from the high frequency components in the image. This technique is probe independent and improves the resolution of optical microscopes by a factor of two. However structured illumination is also limited to widefield microscopy and it relies on complex numerical processing; the necessary multiple acquisitions limit its temporal resolution [8], especially in multicolor imaging [9]. In STED microscopy a scanning excitation spot is overlapped with a doughnut spot of longer wavelength to de-excite fluorophores by stimulated emission [10]. The approach is compatible with fast laser scanning microscopy and potentially yields unlimited resolution.

#188025 - $15.00 USD Received 1 Apr 2013; revised 31 May 2013; accepted 31 May 2013; published 25 Jun 2013

However STED relies on specific properties of fluorophores and involves high saturating laser fluxes, which can cause fluorophores to undergo undesired transitions leading to photo-bleaching and possibly photo-damage [11]. Even in its most recent implementation, gated-STED requires tens of milliwatts of laser power to yield a 4-fold resolution enhancement [12].

Although they provide impressive resolution enhancement, the afore-mentioned methods rely on fluorescence as well as specific photo-physical properties of the molecular probes or require complex optical systems. This affects the deployment of super-resolution microscopy and its applicability to different imaging modalities and sample types. To overcome these limitations, other approaches based on the use of tightly focused radially polarized beams have been developed; it has been demonstrated by Dorn *et al.* that the spot size of a radially polarized beam is smaller than that of a linearly polarized beam when it is tightly focused and its longitudinal field is increased [13]. Some studies have exploited this properties and demonstrated resolution enhancement in laser scanning microscopy using an annular aperture [14], a higher order radially polarized beam [15], or a parabolic mirror as the focusing system [16]. Unfortunately such techniques are only compatible with a specific modality, or cannot be easily retrofitted in conventional laser scanning microscopes.

To simplify the device implementation in laser scanning microscopy (LSM) without probe dependency, we developed a multiplatform approach for laser scanning microscopy based on switching between laser modes. Our approach takes advantage of the fact that the dark spot of a transverse electric laser mode yields a smaller feature size than what can be achieved with any bright laser mode. The method does not rely on fluorescence and can easily be retrofitted in conventional microscopy systems.

2. Switching LAser Mode (SLAM) microscopy: theoretical analysis

In our approach, the sample is first probed with a transverse electric laser mode having a dark spot at its center, henceforth referred to the dark beam. To distinguish the inner part (signal) from the outer part (background) of the dark beam, the sample is also probed with a bright beam having a peak of intensity at its center. A high resolution image is obtained by subtracting the two images. We call this technique Switching LAser Mode (SLAM) microscopy.

In the resulting image, the resolution is no longer defined by the full width at half maximum (FWHM) of the bright spot as in conventional LSM, but by the hole diameter of the dark beam. In our experiments, we used the azimuthally polarized TE_{01} dark mode. This dark mode is still diffraction limited; however its limit is lower than that of a bright mode because it is characterized by an intensity distribution defined by a sum of Bessel functions $J_1(kr\sin\alpha)$, yielding a hole diameter as small as ~λ/4 in contrast to the larger diffraction limits of bright beams (as demonstrated in section 2.3). Subtraction imaging using dark modes to enhance resolution in microscopy has been discussed in a theoretical paper [17], and it has been investigated experimentally with larger and non-symmetrical dark beams [18] introducing distortion in the image obtained by subtraction.

In our approach, a g factor is also introduced in the subtraction procedure to enhance contrast: $PSF^{SLAM} = PSF^{bright} - g \cdot PSF^{dark}$. With increasing g factors, negative values generated beyond the edges of the bright beam are set to zero because they are meaningless. This strategy has the advantage of yielding a physical contrast enhancement without compromising on detection sensitivity. Such a contrast enhancement has the advantage of not depending upon a priori information about the structure being imaged, nor upon the characteristics of the excitation and/or detection systems as opposed to deconvolution methods.

In the following sections, we provide the theoretical arguments explaining why the subtraction scheme improves the resolution when a TE_{01} dark beam is used. We proceed by comparing in the same tight focusing conditions the linearly polarized Gaussian beams used in conventional systems with two main families of dark beams, namely the azimuthally

#188025 - $15.00 USD Received 1 Apr 2013; revised 31 May 2013; accepted 31 May 2013; published 25 Jun 2013

polarized transverse electric modes and the circularly polarized vortex modes. Using those calculations, we evaluated the theoretical PSFs of SLAM microscopy. With this analysis, we also demonstrated that the diffraction limit of the azimuthally polarized TE_{01} mode is smaller than that of the circularly polarized vortex beam used in STED microscopy, making it a better candidate for enhanced resolution imaging using SLAM microscopy. A similar analysis has been done by Khonina *et al.* to find the optimized configuration in STED microscopy [19].

2.1 Theoretical analysis of the tight focusing of bright modes

According to the Rayleigh criterion, the resolution of an optical microscope is limited by diffraction to 1.22λ/(2NA). When a 532-nm laser beam is focused with a 1.2 NA water immersion objective, a resolution of 270 nm is predicted, which corresponds to an Airy disk having a FWHM of 228 nm. However this value is based on the paraxial approximation valid only for low NA objectives. Using high NA objectives, focal spots are deformed by the longitudinal electric field component which is no more negligible compared to the transverse electric field component: the focal spot of the linearly polarized Gaussian beam, used in commercial LSM, becomes elongated in the direction of polarization. This elongation is not incorporated in the Rayleigh criterion valid only along the small axis of the point spread function (PSF), and it decreases the effective resolution by approximately 30%, as will be shown later (e. g. Fig. 3).

To evaluate the intensity distribution at the focus of a high numerical aplanetic lens, we use the vectorial diffraction theory developed by Richards and Wolf [20,21]. The electric field $\mathbf{E}(r,\phi,z)$ near focus is expressed in cylindrical coordinates (r,ϕ,z) as a superposition of plane waves $\exp(j\mathbf{k}\bullet\mathbf{r})$ with different amplitudes (see Fig. 1):

$$\mathbf{E}(r,\phi,z)=\frac{E_o}{2\pi}\iint_{\Omega} q(\alpha)\mathbf{A}(\alpha,\beta)\exp\left(j\mathbf{k}\bullet\mathbf{r}\right)\mathrm{d}\Omega, \tag{1}$$

where $\mathbf{A}(\alpha,\beta)\equiv \ell_0(\alpha,\beta)\hat{\mathbf{a}}(\alpha,\beta)$ is the vector field amplitude after refraction by the focusing lens, $\ell_0(\alpha,\beta)$ is the amplitude distribution at the entrance pupil and $\hat{\mathbf{a}}(\alpha,\beta)$ a unit vector aligned with the direction of polarization, α and β are the polar and the azimuthal angles of the incident plane wave component, respectively, E_o is a constant amplitude, **k** is the wave vector oriented toward the focus, **r** is the position vector, and $\mathrm{d}\Omega=\sin\alpha\mathrm{d}\alpha\mathrm{d}\beta$ is the element of solid angle Ω that covers the entrance pupil of the focusing system. The apodization factor $q(\alpha)=1/\sqrt{n}\cos\alpha^{1/2}$ is imposed by energy conservation after focusing by the lens.

The cartesian components of each wave vector **k** of the converging beam are respectively given by $k_x=k\sin\alpha\cos\beta$, $k_y=k\sin\alpha\sin\beta$ and $k_z=k\cos\alpha$, where $k\equiv|\mathbf{k}|=2\pi n/\lambda$ is the wave number, λ is the wavelength in free space and n is the refractive index of the medium in which the beam is focused. Therefore, $\mathbf{k}\bullet\mathbf{r}=kz\cos\alpha+kr\sin\alpha\cos(\phi-\beta)$.

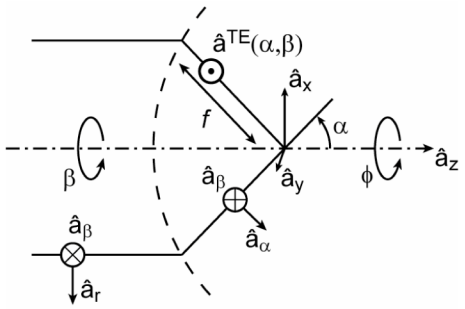

Fig. 1. Geometry of the aplanetic lens (microscope objective) and definitions of the coordinates used in the theoretical analysis.

#188025 - $15.00 USD Received 1 Apr 2013; revised 31 May 2013; accepted 31 May 2013; published 25 Jun 2013

We consider now the focusing of a fundamental TEM_{00} bright beam polarized along the x direction at the entrance pupil of the focusing lens ($\hat{\mathbf{a}}_{\text{incident}} = \hat{\mathbf{a}}_x$). The incident amplitude is azimuthally symmetric:

$$\ell_0(\alpha,\beta) = \exp(-(f\sin\alpha)^2 / w^2), \tag{2}$$

where f is the focal length of the focusing system and w the waist of the incident laser beam. The polarization vector after refraction by the focusing system is given by:

$$\begin{aligned}\hat{\mathbf{a}}(\alpha,\beta) &= \left[\hat{\mathbf{a}}_x \bullet \hat{\mathbf{a}}_r\right]\hat{\mathbf{a}}_\alpha + \left[\hat{\mathbf{a}}_x \bullet \hat{\mathbf{a}}_\beta\right]\hat{\mathbf{a}}_\beta \\ &= \hat{\mathbf{a}}_\alpha(\alpha,\beta)\cos\beta - \hat{\mathbf{a}}_\beta(\beta)\sin\beta,\end{aligned} \tag{3a}$$

$$\begin{aligned}\hat{\mathbf{a}}(\alpha,\beta) = \hat{\mathbf{a}}_x &\frac{1}{2}\left[(\cos\alpha+1)+(\cos\alpha-1)\cos 2\beta\right] \\ &+\hat{\mathbf{a}}_y \frac{1}{2}(\cos\alpha-1)\sin 2\beta \\ &-\hat{\mathbf{a}}_z \sin\alpha\cos\beta,\end{aligned} \tag{3b}$$

where $\hat{\mathbf{a}}_r = \hat{\mathbf{a}}_x\cos\beta + \hat{\mathbf{a}}_y\sin\beta$. The cartesian coordinates of the unit vectors $\hat{\mathbf{a}}_\alpha$ and $\hat{\mathbf{a}}_\beta$ after refraction by the objective lens are:

$$\hat{\mathbf{a}}_\alpha(\alpha,\beta) = \hat{\mathbf{a}}_x\cos\alpha\cos\beta + \hat{\mathbf{a}}_y\cos\alpha\sin\beta - \hat{\mathbf{a}}_z\sin\alpha, \tag{4a}$$

$$\hat{\mathbf{a}}_\beta(\beta) = -\hat{\mathbf{a}}_x\sin\beta + \hat{\mathbf{a}}_y\cos\beta, \tag{4b}$$

$\hat{\mathbf{a}}_x, \hat{\mathbf{a}}_y, \hat{\mathbf{a}}_z$ are the unit vectors oriented along the Cartesian axes x, y, z. Using Eq. (3a), the Richards–Wolf integral equation (Eq. (1)) can be rewritten as:

$$\begin{aligned}\mathbf{E}(r,\phi,z) = \frac{E_o}{2\pi\sqrt{n}}&\int_0^{2\pi}\int_0^{\alpha_{\max}} \cos\alpha^{1/2}\exp(-(f\sin\alpha)^2/w^2)\ \sin\alpha \\ &\times\left(\hat{\mathbf{a}}_\alpha\cos\beta - \hat{\mathbf{a}}_\beta\sin\beta\right)\exp\left[jk\left(z\cos\alpha + r\sin\alpha\cos(\phi-\beta)\right)\right]\mathrm{d}\alpha\,\mathrm{d}\beta,\end{aligned} \tag{5}$$

where $\alpha_{\max}$ is the maximum focusing angle related to the numerical aperture (NA) of the focusing system by $NA = n\sin\alpha_{\max}$. The integration over β can be carried out using the following identities [21]:

$$\int_0^{2\pi}\exp[j\gamma\cos(\phi-\beta)]\begin{Bmatrix}\cos(m\beta)\\ \sin(m\beta)\end{Bmatrix}\mathrm{d}\beta = 2\pi j^m J_m(\gamma)\begin{Bmatrix}\cos(m\phi)\\ \sin(m\phi)\end{Bmatrix}, \tag{6}$$

where $J_m(\gamma)$ is the Bessel function of the first kind of order m. Substituting Eq. (6) in Eq. (1), one finds that the Cartesian components of electric field of the TEM_{00} laser mode near focus are given by:

$$\begin{aligned}E_x(r,\phi,z) = \frac{E_o}{2\sqrt{n}}&\int_0^{\alpha_{\max}}\cos\alpha^{1/2}\sin\alpha\exp(-(f\sin\alpha)^2/w^2)\exp(jkz\cos\alpha) \\ &\times\left[(1+\cos\alpha)J_0(kr\sin\alpha) + (1-\cos\alpha)J_2(kr\sin\alpha)\cos 2\phi\right]d\alpha,\end{aligned} \tag{7a}$$

$$\begin{aligned}E_y(r,\phi,z) = \frac{E_o}{2\sqrt{n}}&\int_0^{\alpha_{\max}}\cos\alpha^{1/2}\sin\alpha\exp(-(f\sin\alpha)^2/w^2)\exp(jkz\cos\alpha) \\ &\times(1-\cos\alpha)J_2(kr\sin\alpha)\sin 2\phi\, d\alpha,\end{aligned} \tag{7b}$$

#188025 - $15.00 USD Received 1 Apr 2013; revised 31 May 2013; accepted 31 May 2013; published 25 Jun 2013

$$E_z(r,\phi,z) = -j\frac{E_o}{\sqrt{n}}\int_0^{\alpha_{\max}} \cos\alpha^{1/2}\sin\alpha^2 \exp(-(f\sin\alpha)^2/w^2)\exp(jkz\cos\alpha) \times J_1(kr\sin\alpha)\cos\phi d\alpha. \quad (7c)$$

Equations (7) give the three Cartesian components of the electric field of a linearly polarized Gaussian beam focused with a high numerical aperture objective.

If a coverslip is being used and if the laser beam is focused at the "coverslip/mounting medium" interface, we also have to consider the longitudinal field enhancement. When a laser beam is focused at a flat interface located on the z-axis, the properties of its field components verify the boundary conditions [22]:

$$E_x^{\text{coverslip}} = E_x^{\text{medium}}, \quad (8a)$$

$$E_y^{\text{coverslip}} = E_y^{\text{medium}}, \quad (8b)$$

$$\varepsilon_{\text{coverslip}} E_z^{\text{coverslip}} = \varepsilon_{\text{medium}} E_z^{\text{medium}}. \quad (8c)$$

For instance, with $n_{\text{coverslip}} = 1.5$ and $n_{\text{medium}} = 1.4$, the longitudinal intensity $|E_z|^2$ is increased by a factor 1.32 from one side of the interface to the other side. Equations (8) give the three Cartesian components of the electric field of a linearly polarized TEM_{00} mode (Gaussian mode) focused without coverslip with a high numerical aperture objective. The effect of a coverslip can also be calculated by substituting Eqs. (7) in Eqs. (8).

2.2 Theoretical analysis of the tight focusing of dark modes

To compare the spot size of bright and dark beams, we consider now the focusing of an azimuthally polarized transverse electric mode. To avoid artifacts due to the multiple rings of higher order transverse electric modes, we studied the first-order TE_{01} laser mode. Its amplitude after refraction by the lens is $l_0(\alpha) = (f\sin\alpha/w)\exp(-(f\sin\alpha)^2/w^2)$, and its electric field is oriented azimuthally with respect to the optical axis: $\mathbf{A}(\alpha) = l_0(\alpha)\hat{\mathbf{a}}_\beta$. The Richards–Wolf integral Eq. (1) then becomes:

$$\mathbf{E}(r,\phi,z) = \frac{E_o}{2\pi}\int_0^{2\pi}\int_0^{\alpha_{\max}} q(\alpha)\ell_0(\alpha)\left(-\hat{\mathbf{a}}_x\sin\beta + \hat{\mathbf{a}}_y\cos\beta\right) \times \exp\left[jk\left(z\cos\alpha + r\sin\alpha\cos(\phi-\beta)\right)\right]\sin\alpha\,\mathrm{d}\alpha\,\mathrm{d}\beta. \quad (9)$$

The integration over β can be carried out by substituting Eq. (6) in Eq. (9), and one finds that the electric field of the TE_{01} laser mode near focus is given by:

$$\mathbf{E}(r,z) = j\frac{E_o}{\sqrt{n}}\frac{f}{w}\hat{\mathbf{a}}_\phi\int_0^{\alpha_{\max}} \cos\alpha^{1/2}\sin\alpha^2\exp(-(f\sin\alpha)^2/w^2) \times J_1(kr\sin\alpha)\exp(jkz\cos\alpha)\,\mathrm{d}\alpha, \quad (10)$$

where $\hat{\mathbf{a}}_\phi(\phi) = -\hat{\mathbf{a}}_x\sin\phi + \hat{\mathbf{a}}_y\cos\phi$ is the azimuthal unit vector in cylindrical coordinates. Equation (10) gives the expression of the electric field of a TE_{01} laser mode at the focus of a high numerical aperture objective.

To compare the spot sizes of azimuthally polarized modes and vortex modes, we also use the same analysis to calculate the electric field of the circularly polarized vortex mode used in Stimulation Emission Depletion (STED) microscopy. We studied the vortex mode of topological charge + 1, because the spot size of vortex modes increases with the topological charge. Its amplitude at the entrance pupil of the focusing lens is given by:

$$\ell_0(\alpha,\beta) = \frac{f\sin\alpha}{w}e^{j\beta}\exp(-(f\sin\alpha)^2/w^2). \quad (11)$$

#188025 - $15.00 USD Received 1 Apr 2013; revised 31 May 2013; accepted 31 May 2013; published 25 Jun 2013

For a right hand circularly polarized incident beam ($\hat{\mathbf{a}}_{\text{incident}} = \hat{\mathbf{a}}_x + j\hat{\mathbf{a}}_y$), the polarization vector after refraction by the focusing system is:

$$\begin{aligned}\hat{\mathbf{a}}(\alpha,\beta) &= \left[(\hat{\mathbf{a}}_x + j\hat{\mathbf{a}}_y)\bullet\hat{\mathbf{a}}_r\right]\hat{\mathbf{a}}_\alpha + \left[(\hat{\mathbf{a}}_x + j\hat{\mathbf{a}}_y)\bullet\hat{\mathbf{a}}_\beta\right]\hat{\mathbf{a}}_\beta \\ &= e^{j\beta}(\hat{\mathbf{a}}_\alpha(\alpha,\beta) + j\hat{\mathbf{a}}_\beta(\beta)),\end{aligned} \tag{12a}$$

$$\begin{aligned}\hat{\mathbf{a}}(\alpha,\beta) = {} & \hat{\mathbf{a}}_x e^{j\beta}(\cos\alpha\cos\beta - j\sin\beta) \\ & + \hat{\mathbf{a}}_y e^{j\beta}(\cos\alpha\sin\beta + j\cos\beta) \\ & - \hat{\mathbf{a}}_z e^{j\beta}\sin\alpha,\end{aligned} \tag{12b}$$

where $\hat{\mathbf{a}}_r = \hat{\mathbf{a}}_x\cos\beta + \hat{\mathbf{a}}_y\sin\beta$. Using Eq. (12a), the Richards–Wolf integral equation can be rewritten as:

$$\begin{aligned}\mathbf{E}(r,\phi,z) = {} & \frac{E_o}{2\pi\sqrt{n}}\frac{f}{w}\int_0^{2\pi}\int_0^{\alpha_{\max}}\cos\alpha^{1/2}\sin\alpha^2 e^{2j\beta}\exp(-(f\sin\alpha)^2/w^2) \\ & \times(\hat{\mathbf{a}}_\alpha(\alpha,\beta) + j\hat{\mathbf{a}}_\beta(\beta))\exp\left[jk\left(z\cos\alpha + r\sin\alpha\cos(\phi-\beta)\right)\right]\mathrm{d}\alpha\,\mathrm{d}\beta.\end{aligned} \tag{13}$$

Using Eqs. (6), the following relations can be established:

$$\int_0^{2\pi}\exp[j\gamma\cos(\phi-\beta)]e^{j2\beta}\cos\beta\,\mathrm{d}\beta = \pi j J_1(\gamma)\ e^{j\phi} - \pi j J_3(\gamma)\ e^{j3\phi}, \tag{14a}$$

$$\int_0^{2\pi}\exp[j\gamma\cos(\phi-\beta)]e^{j2\beta}\sin\beta\,\mathrm{d}\beta = -\pi J_1(\gamma)\ e^{j\phi} - \pi J_3(\gamma)\ e^{j3\phi}. \tag{14b}$$

The integration over β can then be carried out using using Eqs. (6), (12b) and (14). Cartesian components of the electric field near focus are given by:

$$\begin{aligned}E_x(r,\phi,z) = {} & j\frac{E_o}{2\sqrt{n}}\frac{f}{w}\int_0^{\alpha_{\max}}\cos\alpha^{1/2}\sin\alpha^2\exp(-(f\sin\alpha)^2/w^2)\exp(jkz\cos\alpha) \\ & \times\left[(1+\cos\alpha)J_1(kr\sin\alpha)\ e^{j\phi} + (1-\cos\alpha)J_3(kr\sin\alpha)\ e^{j3\phi}\right]d\alpha,\end{aligned} \tag{15a}$$

$$\begin{aligned}E_y(r,\phi,z) = {} & \frac{E_o}{2\sqrt{n}}\frac{f}{w}\int_0^{\alpha_{\max}}\cos\alpha^{1/2}\sin\alpha^2\exp(-(f\sin\alpha)^2/w^2)\exp(jkz\cos\alpha) \\ & \times\left[-(1+\cos\alpha)J_1(kr\sin\alpha)\ e^{j\phi} + (1-\cos\alpha)J_3(kr\sin\alpha)\ e^{j3\phi}\right]d\alpha,\end{aligned} \tag{15b}$$

$$\begin{aligned}E_z(r,\phi,z) = {} & \frac{E_o}{\sqrt{n}}\frac{f}{w}\int_0^{\alpha_{\max}}\cos\alpha^{1/2}\exp(-(f\sin\alpha)^2/w^2)\exp(jkz\cos\alpha) \\ & \times\sin\alpha^3 J_2(kr\sin\alpha)\ e^{j2\phi}d\alpha.\end{aligned} \tag{15c}$$

Equations (15) give the three Cartesian components of the electric field of a circularly polarized vortex mode focused without coverslip with a high numerical aperture objective. The effect of a coverslip can also be calculated by substituting Eqs. (15) in Eqs. (8).

2.3 Comparison between the theoretical spot sizes of dark and bright modes

From Eqs. (7), (8), (10) and (15), we now compute the electric field of linearly polarized bright beams and of azimuthally polarized or circularly polarized dark beams, with three high numerical aperture objectives: a 1.4 NA oil immersion objective, a 1.2 NA water immersion objective, and the theoretical case of $\pi/2$ focusing in air. A mounting medium having a 1.4 refractive index is also used to reproduce experimental conditions with oil and water immersion objectives (see Section 3).

#188025 - $15.00 USD Received 1 Apr 2013; revised 31 May 2013; accepted 31 May 2013; published 25 Jun 2013

In Table 1, the hole diameters at half maximum of dark beams are compared with the full width at half maximum (FWHM) of a linearly polarized Gaussian beam focused under the same conditions.

Table 1. Comparison between theoretical dark beam and bright beam diameters

	1.4 NA (oil)	1.2 NA (water)	1 NA (air)
dark beams			
TE_{01}	0.25λ	0.30λ	0.35λ
vortex	0.30λ	0.33λ	0.40λ
bright beam			
TEM_{00} (small axis)	0.35λ	0.44λ	0.49λ
TEM_{00} (large axis)	0.58λ	0.57λ	0.75λ

The azimuthally polarized mode used here as a dark mode is still diffraction limited. However the diffraction limit of its central dark spot is lower than that of a bright beam; its intensity distribution is defined by a sum of Bessel functions $J_1(kr\sin\alpha)$ (see Eq. (10)), yielding a hole diameter as small as ~λ/4 in contrast to the larger diffraction limits of Gaussian bright beams. For comparison, the circularly polarized vortex mode involves a combination of Bessel functions $J_1(kr\sin\alpha)$, $J_2(kr\sin\alpha)$, and $J_3(kr\sin\alpha)$ (Eq. (15)), producing a larger hole diameter (~λ/3.3). This confirms that the TE_{01} laser mode is a better candidate for resolution enhancement using SLAM microscopy.

For instance, with a 1.4 NA oil immersion objective and a mounting medium having a 1.4 refractive index, the spot size is reduced by a factor up to 2.3 from the bright mode to the azimuthally polarized dark mode (Table 1). As the size of the PSF in SLAM microscopy is very similar to the hole size of the dark beam used for the subtraction, a PSF with a diameter as small as ~λ/4 can then be achieved with this approach; an improvement of this magnitude cannot be achieved using a circularly polarized vortex mode. Moreover, the ellipticity created by the elongated spot sizes of the linearly polarized Gaussian beam is reduced when SLAM is used, preserving the shape of the observed structures as will be shown later (see Fig. 6(a)).

2.4 Theoretical demonstration of resolution enhancement using SLAM

To evaluate theoretically the impact of the subtraction scheme on the resolution enhancement of SLAM microscopy, we first compared the size of the point spread functions obtained in confocal microscopy before (Figs. 2(a) and 2(b)) and after the subtraction process (Fig. 2(c)). With a 1.4 NA oil immersion objective and a g factor of 0.65, the spot size of the tightly focused circularly polarized Gaussian beam is reduced from 0.46λ to 0.25λ (Fig. 2(e)). In comparison the spot size of the linearly polarized Gaussian beam is reduced from 0.58λ to 0.29λ in the direction of the polarization (large axis), and from 0.35λ to 0.22λ in the direction perpendicular to the polarization (small axis). The size of the overall PSF is then reduced by a factor of approximately two using SLAM microscopy.

We can notice in Fig. 2(d) that the subtraction process creates negative values around the object, which is a point source in this case. As the object is always represented by a maximum of intensity in the bright image and a minimum of intensity in the dark image, the negative values fall outside the object (Fig. 2(d)). They are therefore meaningless and can be set to zero (Fig. 2(e)). However a high contrast enhancement (high value of the g factor) introduces large negative values, which can deteriorate the quality of information. As in any contrast enhancement approaches, one must be careful when very intense structures are located close to weaker ones. To avoid exaggerated contrast enhancement, in our experiments we generally used g factors around 0.65, and never used one above 1.

#188025 - $15.00 USD Received 1 Apr 2013; revised 31 May 2013; accepted 31 May 2013; published 25 Jun 2013

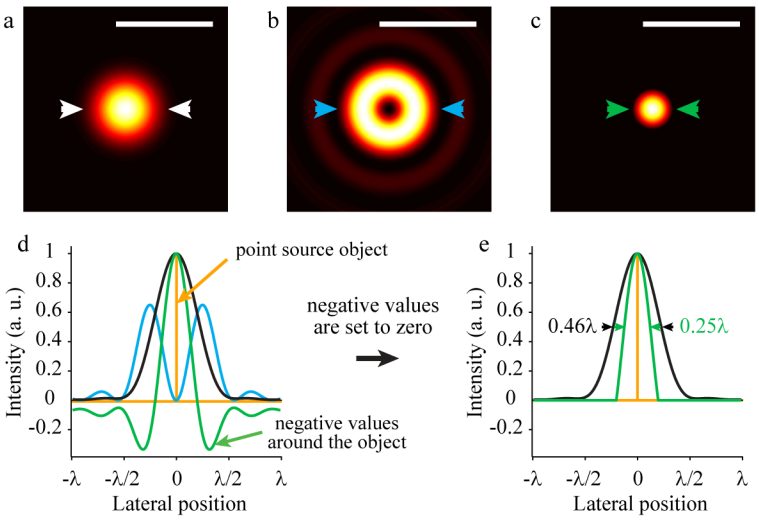

Fig. 2. Theoretical calculation of the point spread function obtained in SLAM microscopy with a 1.4 NA oil immersion objective in the mounting medium. (a) PSF obtained with a circularly polarized Gaussian beam. (b) PSF obtained with the azimuthally polarized TE_{01} laser beam. (c) PSF of SLAM microscopy using theoretical PSFs given in (a) and (b) and a g factor of 0.65. (d,e) Intensity profiles along the horizontal direction of the PSFs obtained with the Gaussian beam (black), the TE_{01} laser beam (blue) and SLAM (green). In (e), the negative values introduced by the subtraction process are set to zero because they do not have a physical meaning and are created outside of the object. Scale bar: λ.

To demonstrate theoretically that SLAM microscopy can reveal new features. We calculated the images of four point sources using Gaussian beams (Figs. 3(a)-3(c), and 3(e)) and azimuthally polarized beams (convolution of the four point sources with the theoretical PSFs). To theoretically predict the resolution enhancement of our experimental setup (see section 3.1), we calculated the PSFs for a 1.2 NA water immersion objective and an excitation wavelength of 532 nm. The calculations were performed using the diffraction theory established by Richards and Wolf (Eqs. (7), (8), and (10)).

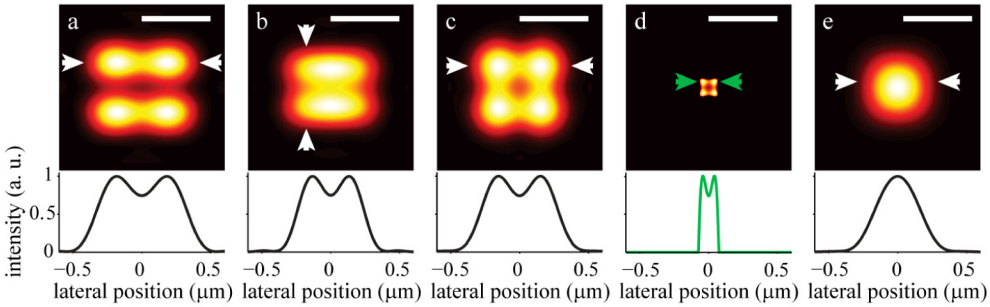

Fig. 3. Theoretical calculation of resolution enhancement using SLAM microscopy. Theoretical images of four point sources using (a,b,c,e) conventional confocal imaging and (d) confocal SLAM microscopy. (a) Image obtained with a linearly polarized Gaussian beam of point sources separated by the limit of resolution along the direction of polarization. (b) Same as (a), for the resolution limit along the perpendicular direction. (c) Same as (a) and (b), but for a circularly polarized Gaussian beam. (d) Image obtained at the resolution limit of SLAM microscopy; (e) image obtained of the same four point sources as in (d) using conventional confocal microscopy. Scale bar 500 nm. (a-d) The resolution limits were defined by a 75% contrast between the peaks and the valley between the peaks.

By changing the distance between the four points, we compared the diffraction limit of conventional imaging (Figs. 3(a)-3(c) and 3(e)) with SLAM microscopy (Fig. 3(d)):

#188025 - $15.00 USD Received 1 Apr 2013; revised 31 May 2013; accepted 31 May 2013; published 25 Jun 2013

resolution is improved by a factor of up to 2.15 compared to that obtained with a linearly polarized Gaussian beam, and a factor of 1.85 compared to that obtained with a circularly polarized Gaussian beam. The resolution limits were defined by a 75% contrast between the peaks and the valley between the peaks. The resolution enhancement is evident when we compare confocal and SLAM images of the same structure (Fig. 3(d) versus Fig. 3(e)).

To experimentally validate the theoretical predictions, we implemented the SLAM process with three different modalities, a confocal reflectance microscope, a confocal fluorescence microscope, and a two-photon excited fluorescence microscope; we also compared the values with that obtained with scanning electron microscopy (SEM).

3. Experimental results with two laser scanning microscopes

3.1 Experimental setup

In a conventional LSM, the sample is scanned with a linearly polarized Gaussian beam. In our experiments, we added two components in the optical path: a mode converter to convert the Gaussian laser beam into an azimuthally polarized laser beam and an optical switch based on rotating mirrors (Fig. 4). Using fast rotating mirrors, switching can be achieved either line-by-line or image-by-image without limiting temporal resolution by a factor larger than two. A line-by-line switching would limit artifacts due to sample motion in live cell imaging.

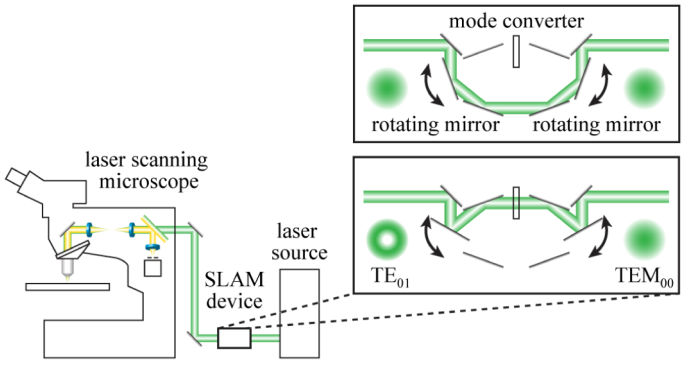

Fig. 4. Experimental setup for SLAM microscopy. Two components are placed between the laser source and the microscope: a mode converter to convert the Gaussian laser beam into an azimuthally polarized laser beam, and an optical switch based on rotating mirrors.

In our experiments, we took advantage of the fact that tunable TE_{01} laser mode generators are available. For confocal measurements, a liquid-crystal-based mode converter was chosen for its tunability (ARCoptix, Switzerland). For two-photon experiments, we used a monolithic assembly consisting of low order half-wave plates made of crystalline quartz layed out in four quadrants and a π-phase shift plate (J.Fichou, Fresnes, France) to limit dispersion effects.

Experiments were conducted in a custom-designed confocal microscope (using *Scanimage* software [23]) and a commercial two-photon fluorescence excited microscope (LSM 510, Zeiss, Germany). To demonstrate that SLAM microscopy is fully retrofittable in commercial systems, the two-photon experiments have been conducted by simply inserting the SLAM components between the Ti:Sapphire laser (Chameleon, Coherent, United States) and the microscope.

3.2 Experimental results in reflectance confocal microscopy

To experimentally demonstrate that resolution is enhanced in confocal microscopy using the SLAM process, we first imaged the same pattern in confocal reflectance microscopy and scanning electron microscopy (SEM). The sample is a random distribution of 100-nm diameter gold nano-particles (NanoComposix, United States). A low concentration of particles was deposited on a poly-D-lysine coated coverslip. After evaporation of the solution,

#188025 - $15.00 USD Received 1 Apr 2013; revised 31 May 2013; accepted 31 May 2013; published 25 Jun 2013

the dried nano-particles were imaged with a commercial SEM having a spatial resolution of 1.5 nm (Quanta 3D FEG, FEI, United States) (Fig. 5(a)).

The gold nano-particles were then immersed in water and imaged by focusing a linearly polarized Gaussian beam at 532 nm with a 1.2 NA water immersion objective (Fig. 5(b)). When observing single particles, the FWHM of the reflectance PSF was limited by diffraction to 230 nm in the direction perpendicular to the polarization (small axis). This result is in agreement with the theoretical predictions (see section 2.1). The same particles were also imaged with the TE_{01} laser beam to obtain the confocal reflectance SLAM image (Fig. 5(c)).

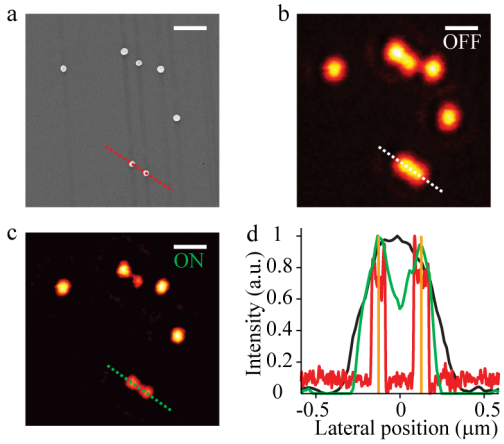

Fig. 5. Experimental demonstration of resolution enhancement using SLAM microscopy: comparison between images of sparsely dispersed 100-nm diameter gold nano-particles imaged by (a) scanning electron microscopy, (b) conventional reflectance microscopy ("OFF") and (c) SLAM microscopy ("ON"). (d) Intensity profiles evaluated along two close nano-particless in SEM (red), reflectance microscopy (dark) and SLAM reflectance microscopy (green). The orange lines indicate the centers of the nano-particless in the SEM image. Scale bars: 500 nm.

The resolution enhancement becomes evident when comparing the images of two close nano-particles (dotted lines in Figs. 5(a)-5(c)). In Fig. 5(d), we compared the intensity profiles evaluated along those dotted lines in the SEM image (red), the conventional reflectance image (dark), and the SLAM reflectance image (green). The orange lines indicate the centers of the beads evaluated using the SEM data. As the maxima of the SLAM profile point exactly on those lines, this result confirms that SLAM imaging reveals new structures invisible in conventional imaging, and gives their localization with accuracy.

These results using reflectance microscopy show that SLAM imaging is compatible with non-fluorescent modalities. SLAM microscopy thus opens avenues for resolution enhancement for a multitude of non-invasive laser scaning imaging modalities including second- and third- harmonics generation microscopy [24] or coherent anti-Stokes Raman scattering microscopy [25].

3.3 Experimental results in fluorescence confocal microscopy

To demonstrate that resolution is also improved in fluorescence confocal microscopy, we imaged 100-nm diameter fluorescent nano-beads immersed in a mounting medium with a 1.2 NA water immersion objective. The beads have an excitation maximum at 540 nm. When imaging single beads, the confocal PSF is limited by diffraction to 230-nm which yields 250-nm spots when convolved with the 100-nm diameter beads; experimental profiles are well fitted with numerical calculations (Fig. 6(a)). Using SLAM microscopy, the spot size was considerably reduced (Fig. 6(a)); the resolution enhancement became more evident when imaging beads within dense clusters (Figs. 6(b) and 6(c)).

#188025 - $15.00 USD Received 1 Apr 2013; revised 31 May 2013; accepted 31 May 2013; published 25 Jun 2013

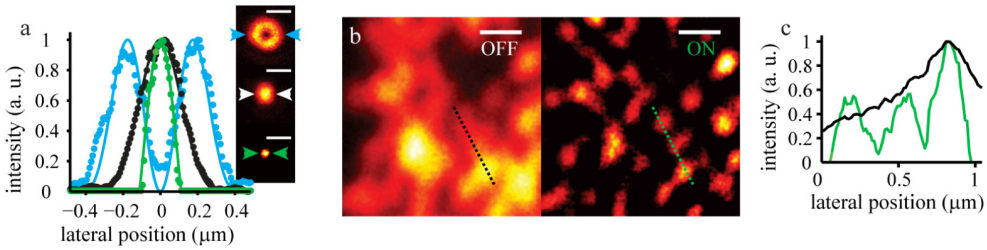

Fig. 6. Experimental characterization of resolution enhancement using confocal SLAM microscopy: images of 100-nm diameter fluorescent beads. (a) Experimental (dotted lines) and theoretical (solid lines) images of bright beam (dark), dark beam (blue) and SLAM (green). The intensity profiles were evaluated along the direction perpendicular to the polarization. (b,c) Demonstration of resolution enhancement with a higher concentration of beads: comparison between conventional confocal microscope ("OFF") and confocal SLAM images ("ON") Scale bars: 500 nm.

We then imaged microtubules of cultured hippocampal neurons revealed by immunohistochemical labeling of tubulin (Figs. 7(a) and 7(b)). At 13 to 15 days in vitro, cultured cells were fixed in 4% PFA and labeled by immunochemistry using a mouse anti-beta-tubulin antibody (Developmental Studies Hybridoma Bank, United States) followed by detection using an alexa 546-conjugated goat anti-mouse antibody (Life Technologies, United States) as described in [26]. We also compared images of cultured neurons expressing mRuby [27] as a structural dye (Figs. 7(c) and 7(d)). Cultured cells were transfected at 13 to 15 days in vitro using Lipofectamine 2000 (Life Technologies, United States), and fixed in 4% paraformaldehyde (PFA) as previously described [26]. For both labeling, coverslips were mounted in Prolong Gold Antifade mounting media (Life Technologies, United States). In all experiments, the continuous wave (CW) excitation power (λ = 532 nm) of both laser beams was maintained bellow 1 μW on the samples to avoid photo-damage.

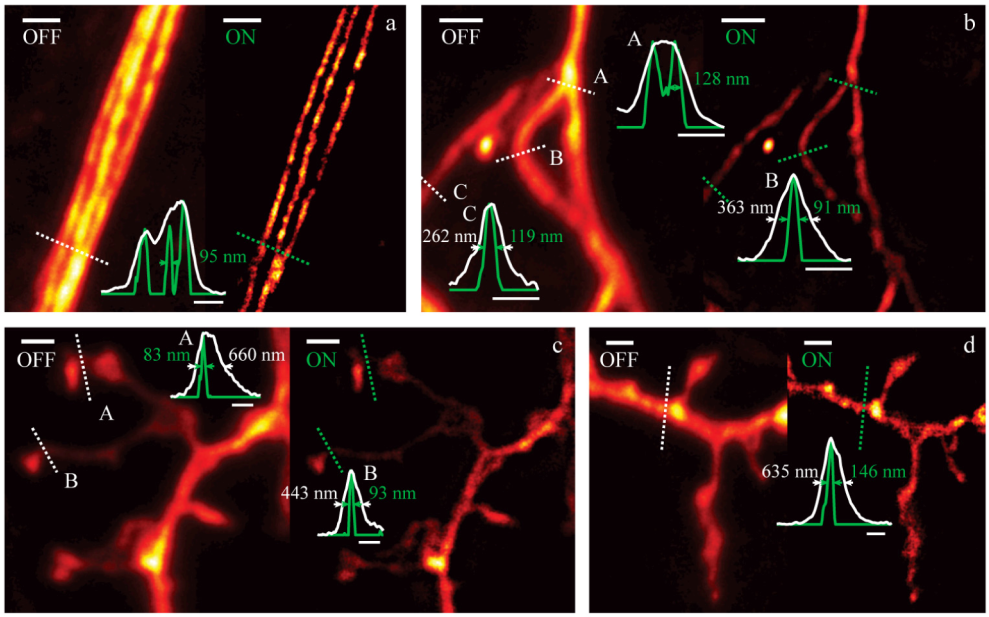

Fig. 7. Resolution and contrast enhancement in cell cultures: comparison between conventional confocal microscope ("OFF") and confocal SLAM images ("ON"). (a,b) Tubulin labeling of neurons by immunohistochemistry (Alexa 546); detection of new features (close fibers) using SLAM microsopy. (c,d) m-Ruby transfected neurons; improved dendritic spine morphology analysis with SLAM microscopy. Image scale bars: 1 μm. Profile scale bars: 500 nm.

#188025 - $15.00 USD Received 1 Apr 2013; revised 31 May 2013; accepted 31 May 2013; published 25 Jun 2013

With a FWHM between 100 nm and 130 nm using SLAM microscopy, close bundles of microtubules in the cytoskeleton of cultured neurons can be revealed (Figs. 7(a) and 7(b)). For instance, in Fig. 7(a), where we plot the intensity profile in the direction perpendicular to the orientation of tubulin fibers, clusters of fibers present in conventional imaging ("OFF" image and white profile) are well differentiated using SLAM imaging ("ON" image and green profile). Spine morphology analysis was also strongly improved (Figs. 7(c) and 7(d)), especially at the junction between spine heads and their necks, which cannot be well resolved using diffraction limited confocal microscopy because the feature size is less than 100 nm. For instance, in Fig. 7(c), the positioning of the spine neck is much more precise using the SLAM procedure (see intensity profile A).

3.4 Experimental results with two-photon excited fluorescence microscopy

To demonstrate that SLAM microscopy is compatible with other modalities, we integrated a mode converter in a commercial two-photon microscope (LSM 510, Zeiss, Germany). Two-photon absorption has the effect of broadening the dark central zone of the TE_{01} laser beam (excitation proportional to the intensity squared [28]). Despite that broadening, the predicted resolution of the microscope still shows improvement by a factor of 1.6. To experimentally characterize the resolution enhancement, we imaged 100-nm diameter fluorescent beads with a 1.2 NA objective at different concentrations. The beads have an excitation maximum at 505 nm and were two-photon excited at 810 nm. Considering the bead diameter, a resolution of 290 nm is achieved in conventional microscopy (Fig. 8(a)); single beads were separated using SLAM two-photon microscopy (Figs. 8(b) and 8(c)). Here again, the experimental PSFs are well fitted with numerical calculation (Fig. 8(a)).

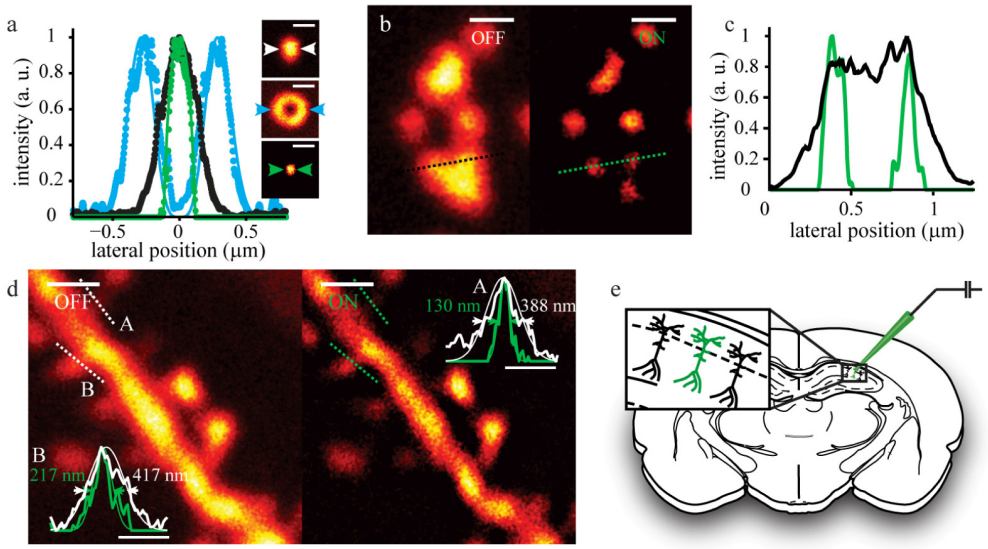

Fig. 8. Two-photon SLAM imaging. (a) Experimental (dotted lines) and theoretical (solid lines) intensity profiles of bright beam (dark), dark beam (blue) and SLAM (green) evaluated along the direction perpendicular to the polarization. (b,c) Demonstration of resolution enhancement with clusters of fluorescent beads: comparison between conventional two-photon excitation microscopy ("OFF") and two-photon SLAM images ("ON"). (d) Two-photon imaging of neuronal dendritic spines in 250-μm thick brain slices. (e) Hippocampal pyramidal neurons were labeled by micro-injection of Lucifer-Yellow. (a,b) Scale bar: 500 nm. (d) Image scale bars: 1 μm. Profile scale bars: 500 nm.

To test the suitability of SLAM microscopy for deep tissue imaging, we improved the analysis of neuronal dendritic spines in 250-μm thick brain slices (Fig. 8(d)). For those experiments, mice were anaesthetized and perfused intracardially with 4% PFA, and brains were postfixed overnight in PFA 4% at 4°C. Single hippocampal neurons were labeled by

#188025 - $15.00 USD Received 1 Apr 2013; revised 31 May 2013; accepted 31 May 2013; published 25 Jun 2013

micro-injection of Lucifer yellow (Life Technologies, United States) as previously described [29]. Several neurons in Dentate gyrus, CA3 or CA1 region of hippocampus were impaled with a micropipette containing Lucifer and injected at 0.5-2nA for 10-15 min to fill the dendritic tree until spines on apical tuft dendrites became clearly visible (Fig. 8(e)). Slices were mounted in the fluorescent mounting medium (Dako, Denmark). The samples were two-photon excited (λ = 810 nm) with a mean power below 3 mW at the surface of the slice to avoid photo-damage.

4. Conclusion

By exploiting the small dark spot of the azimuthally polarized TE_{01} laser beam, a 2.15-fold improvement in resolution was achieved in SLAM microscopy, and a contrast enhancement is obtained without a priori information about the structures being imaged.

If achromatic and/or tunable components are used, the SLAM system can easily be retrofitted in conventional microscopes (custom-designed or commercial units). By definition, SLAM microscopy is also compatible with different modalities and any fluorophore used in conventional confocal and two-photon imaging; it could also be implemented either in micro or macroscopy. In our experiments a laser power not higher than that used in conventional imaging was applied to the samples, to limit photo-bleaching and photo-damage.

Finally, SLAM microscopy opens avenues for resolution enhancement with non-fluorescent imaging modalities such as second- and third-harmonic generation microscopy, coherent anti-Stokes Raman scattering microscopy, or reflectance microscopy.

Acknowledgments

The authors thank Annie Castonguay for support with two-photon experiments, Cyril Bories for brain slices preparation and Lucifer-Yellow micro-injection, Stéphan Gagnon for support in SEM experiments, Francine Nault, Hugues Dufour and Sylvain Côté for expert technical assistance as well as Christian Tardif and Alexandre April for helpful discussions. This work was supported by grants from the Natural Science and Engineering Research Council of Canada to MP and YDK. HD was the recipient of a Scholarship from the Neurophysics Strategic Training Program from the Canadian Institutes of Health Research. YDK was a Chercheur National of the Fonds de la recherche en santé du Québec.